Assessment of deep learning-based PET attenuation correction frameworks in the sinogram domain

Arabi, Hossein; Zaidi, Habib

Published in:
Physics in Medicine and Biology

DOI:
10.1088/1361-6560/ac0e79

Publication date:
2021

Physics in Medicine & Biology

PAPER

Assessment of deep learning-based PET attenuation correction frameworks in the sinogram domain

To cite this article: Hossein Arabi and Habib Zaidi 2021 *Phys. Med. Biol.* **66** 145001

IOP Publishing Phys. Med. Biol. 66 (2021) 145001 https://doi.org/10.1088/1361-6560/ac0e79

Physics in Medicine & Biology

IPEM Institute of Physics and Engineering in Medicine

RECEIVED
20 February 2021

REVISED
11 June 2021

ACCEPTED FOR PUBLICATION
24 June 2021

PUBLISHED
7 July 2021

PAPER

Assessment of deep learning-based PET attenuation correction frameworks in the sinogram domain

Hossein Arabi[1] **and Habib Zaidi**[1,2,3,4]

[1] Division of Nuclear Medicine and Molecular Imaging, Department of Medical Imaging, Geneva University Hospital, CH-1211 Geneva 4, Switzerland
[2] Geneva Neuroscience Center, Geneva University, CH-1205 Geneva, Switzerland
[3] Department of Nuclear Medicine and Molecular Imaging, University of Groningen, University Medical Center Groningen, 9700 RB Groningen, The Netherlands
[4] Department of Nuclear Medicine, University of Southern Denmark, DK-500, Odense, Denmark

E-mail: habib.zaidi@hcuge.ch

Keywords: PET/CT, attenuation correction, machine learning, deep learning, quantification

Supplementary material for this article is available online

Abstract

This study set out to investigate various deep learning frameworks for PET attenuation correction in the sinogram domain. Different models for both time-of-flight (TOF) and non-TOF PET emission data were implemented, including direct estimation of the attenuation corrected (AC) emission sinograms from the nonAC sinograms, estimation of the attenuation correction factors (ACFs) from PET emission data, correction of scattered photons prior to training of the models, and separate training of the models for each segment of the emission sinograms. A segmentation-based 2-class AC map was included as a bottom-line technique for comparison of the different models considering PET/CT AC as reference. Fifty clinical TOF PET/CT brain scans were employed for training whereas 20 were used for evaluation of the models. Quantitative analysis of the resulting PET images was carried out through region-wise standardized uptake value (SUV) bias calculation. The models relying on TOF information significantly outperformed the nonTOF models as well as the segmentation-based AC map resulting in maximum SUV bias of 6.5%, 9.5%, and 14.0%, respectively. Estimation of ACFs from either TOF or nonTOF PET emission data was very sensitive to prior scatter correction. However, direct estimation of AC sinograms from nonAC sinograms revealed no sensitivity to scatter correction, thus obviating the need for prior scatter estimation. For TOF PET data, though direct prediction of the AC sinograms does not require prior estimation of scattered photons, it requires input/output channels equal to the number of TOF bins which might be computationally or memory-wise expensive. Prediction of the ACF matrices from TOF emission data is less demanding in terms of memory as it requires only a single channel for output. AC in the sinogram domain of TOF PET data exhibited superior performance compared to both nonTOF and segmentation-based methods. However, such models require multiple input/output channels.

1. Introduction

Brain positron emission tomography (PET) imaging using ^{18}F-fluorodeoxyglucose (FDG) is commonly carried out in clinical and research settings, wherein quantification plays a critical role in early detection and characterization of brain diseases. Correction for physical degrading factors, such as attenuated and scattered photons is essential to generate clinically relevant and dependable quantitative PET images (Zaidi *et al* 2007).

Attenuation correction (AC) maps derived from computed tomography (CT) images, regarded as the reference or gold standard approach for PET attenuation and scatter corrections on hybrid PET/CT scanners, commonly provide accurate patient-specific information regarding the attenuating media. However, the quantitative imaging capabilities of standalone PET (e.g. dedicated brain/breast) and hybrid PET/MRI scanners

are challenged by the lack of accurate/patient-specific AC map owing to the absence of CT and/or transmission scanning. In the latter case, four generic strategies are commonly employed to generate PET AC maps with or without using structural MR images (Mehranian *et al* 2016). First, classification approaches where MR images are typically segmented into few bulk tissue classes followed by the assignment of predefined linear attenuation coefficients (Martinez-Moller *et al* 2009, Schulz *et al* 2011, Arabi *et al* 2015). Though classification approaches were implemented on commercial systems, the performance of these approaches is limited due to the challenge of bone/air discrimination using conventional MR sequences. The use of advanced MR sequences, such as short- or zero-echo-time (UTE or ZTE), enable the generation of attenuation maps with continuous attenuation coefficients (or bone densities) (Sekine *et al* 2016, Leynes *et al* 2017, Baran *et al* 2018). Atlas-based methods exploit paired MR and CT images to estimate a synthetic CT image for target subjects via an image transformation framework (Wollenweber *et al* 2013, Arabi and Zaidi 2017). In this regard, synthetic CT images could be generated using an established voxel-to-voxel mapping scheme between registered CT atlas images and the target MRI (Arabi and Zaidi 2016, Arabi *et al* 2016). Simultaneous reconstruction of attenuation and activity maps allows for the prediction of patient-specific AC maps from PET emission data (with time-of-flight (TOF) information) (Defrise *et al* 2012). This could be achieved without using structural information; yet, incorporation of the anatomical information (using MRI as prior knowledge) would reduce the ill-posedness of this approach and lead to improved AC maps and/or activity map estimations (Mehranian *et al* 2017). In addition to the aforementioned synthetic CT generation approaches, deep learning algorithms are alternative approaches capable of offering accurate solutions for CT image synthesis from single (Han 2017, Bahrami *et al* 2020) or multiple MR sequences (Emami *et al* 2018, Gong *et al* 2018, Liu *et al* 2018b). These algorithms are widely used in brain, pelvis, and whole-body PET/MR imaging and MRI-only radiation treatment planning (Arabi *et al* 2018, Dinkla *et al* 2018, Leynes *et al* 2018, Arabi *et al* 2019).

Deep learning approaches are widely employed to generate synthetic CT images from MR images for PET attenuation correction on PET/MRI systems (Ladefoged *et al* 2017, Leynes *et al* 2018, Liu *et al* 2018a, Arabi *et al* 2019, Lee 2020, Teuho *et al* 2020, Wang *et al* 2020, Zaidi and El Naqa 2021). The versatility and power of deep learning approaches enabled the implementation of direct attenuation and scatter correction in the image domain, which became feasible without the need for structural images, such as MRI (Yang *et al* 2019, Arabi *et al* 2020, Mostafapour *et al* 2021). In this framework, a deep learning model is trained to convert the non-attenuation corrected PET (PET-nonAC) images to the corresponding CT-based AC PET images (PET-CTAC) via a one-to-one regression scheme.

In addition to the above referenced PET AC approaches, a novel deep learning-based approach was recently introduced to directly estimate the attenuation correction factors (ACFs) from the PET emission data (Arabi and Zaidi 2020). It was demonstrated that PET emission data carry subject-specific information concerning the underlying attenuating medium.

The data representation in the sinogram domain is extremely extended/detailed compared to the image domain. For instance, projections are provided for the different segments (or planes) and TOF information is encoded into a number of separated sinogram bins or matrices. Hence, in the sinogram domain, a wider spectrum of strategies could be adopted to perform attenuation and scatter correction compared to the image domain. In this work, we examine these different strategies and frameworks to perform AC in the sinogram domain using a deep learning approach.

2. Materials and methods

2.1. PET/CT data acquisition

A clinical dataset consisting of 70 TOF PET/CT scans was retrospectively exploited for evaluation of different strategies for deep learning-guided AC in the sinogram domain. Patient scans were carried out on the Biograph mCT PET/CT scanner (Siemens Healthcare, Erlangen, Germany) following intravenous injection of 206 ± 16 MBq of ^{18}F-FDG. PET scans started 31 ± 6 min post-injection for an acquisition time-of 20 min For PET AC, low-dose CT scans were performed using 20 mAs, 120 kVp, 0.3 s rotation speed and $1 \times 1 \times 2.5$ mm^3 voxel size prior to PET scanning. PET emission data were saved in list-mode format to be employed for offline reconstruction of PET data. The e7 tools Siemens reconstruction software was used to generate TOF and nonTOF sinograms from PET list-mode data as well as ACFs, randoms, scatter, and normalization matrices. It should be noted that the mCT scanner is capable of TOF PET imaging with 530 ps coincidence time resolution producing 13 sinograms or TOF bins with a width of 312 ps.

The Biograph mCT scanner and e7 tools enable generating a single nonTOF sinogram of the PET emission data in 9 segments using a matrix of $400 \times 168 \times 621$ elements (bins $\times$ angles $\times$ planes) for each bed acquisition. Considering the TOF information, PET emission data would be generated in 13 sinograms (each in 9 segments and $400 \times 168 \times 621$ elements) corresponding to 13 TOF bins. For both nonTOF and TOF PET

data, a single ACF sinogram would be generated for PET attenuation correction in the same matrix size. Likewise, for normalization, randoms, and scatter corrections, a similar matrix size will be generated for either TOF or nonTOF image reconstruction.

2.2. Deep learning-based attenuation correction strategies in the sinogram domain

Deep learning approaches can be employed to perform AC in the sinogram domain through extracting the ACFs as demonstrated recently by Arabi and Zaidi (2020). This can be carried out in different ways, including considering or not TOF information, extracting the ACFs from PET emission data or generating directly the AC sinograms, considering all segments of the sinogram in a single pipeline or executing the algorithm separately for each segment, performing scatter correction prior to training of the algorithm, and any combination of these choices. In the following sections, these AC strategies in the sinogram domain will be described in detail and evaluated in a common framework to put into perspective their associated advantages and pitfalls.

2.2.1. NonTOF PET data

In the first section, we focus on nonTOF PET emission data and the evaluation of the different AC strategies, which can be implemented in the sinogram domain for nonTOF PET imaging.

2.2.1.1. Estimation of AC sinograms from nonAC sinograms of nonTOF PET data

In this framework, the AC sinograms (AC Sino.) are directly estimated from the nonTOF PET data before attenuation and scatter corrections (nonAC Sino.) using a deep learning model (figure 1(A)). It should be noted that nonAC sinograms refer to PET emission data without attenuation and scatter corrections and after normalization and randoms corrections throughout this manuscript. The input data in this framework is the nonTOF PET emission data corrupted by attenuated and scattered photons where the deep learning model would be trained to estimate/predict attenuation and scatter corrected sinograms.

2.2.1.2. Estimation of ACFs from nonAC sinograms of nonTOF PET data

The same framework was evaluated in our previous study (Arabi and Zaidi, 2020). However, for the sake of completeness, this is included in this work. The input in this framework (figure 1(B)) is also the nonTOF PET data before attenuation and scatter correction (nonAC Sino.) to estimate the corresponding ACF matrix for all 9 segments. The ACF matrix has the same dimension of the PET sinogram ($400 \times 168 \times 621$ elements). Hence, the same deep learning configuration in terms of input and output dimension was used for the implementation of the models shown in figure 1.

2.2.2. TOF PET data

2.2.2.1. Estimation of AC sinograms from nonAC sinograms of TOF PET data

In the previous section, nonTOF PET data were employed to directly estimate AC PET data (AC Sino.) or ACF matrix. For TOF PET data, the same framework can be implemented, except that the TOF PET data are split into 13 sinograms corresponding to 13 time bins. In brain imaging, only 7 out of 13 TOF sinograms contain the PET data corresponding to the subject's head in the field-of-view (FOV) owing to the small size of the brain, whereas the remaining 6 sinograms are almost empty (zero count with some randoms and scattered counts). As such, only the 7 meaningful TOF sinograms were employed to implement AC in the sinogram domain. In figures 2(A), 7 TOF sinograms in 9 segments corresponding to a single bed brain acquisition are supplied to the deep learning model to perform directly AC on the TOF sinograms.

2.2.2.2. Estimation of ACFs from nonAC sinograms of TOF PET data

Similar to the strategies adopted for nonTOF data, the ACF matrix can be estimated from the nonAC sinogram of TOF PET emission data. This framework, illustrated in figure 2(B), was extensively assessed in our previous study (Arabi and Zaidi 2020) and is repeated in this work to ease the comparison to other AC strategies in the sinogram domain. The training of this model is performed using all 9 segments together (with no separate training for each of these segments).

2.2.3. Separation of sinogram segments

In the abovementioned frameworks, the training of the models, either TOF or nonTOF PET data, was carried out using all 9 sinogram segments together. However, the training and assessment of these models could be undertaken separately for each of the 9 segments. The Biograph mCT PET scanner produces sinograms in 9 segments corresponding to direct (first segment) and oblique (segments 2–9 with different projection angles) planes. The first segment (direct plane) contains 109 slices (in z direction), the second and third segments (with

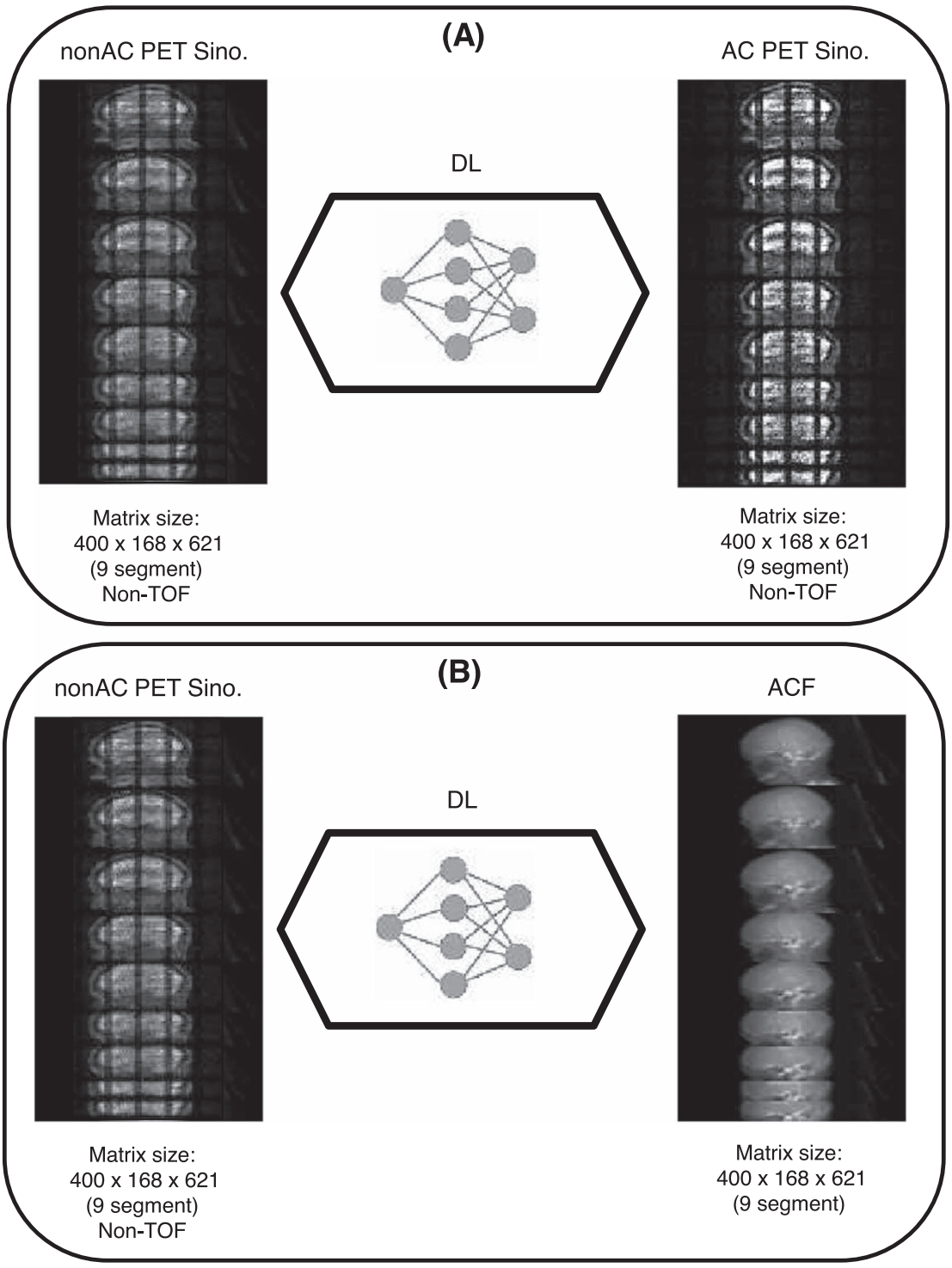

Figure 1. (A) Direct estimation of the attenuation corrected sinogram (AC Sino.) from nonAC nonTOF PET data and (B) ACFs estimation from nonTOF PET sinograms using all 9 segments.

the same opposite projection angles) 96 slices, the 4th and 5th segments 76 slices, the 6th and 7th 54 slices, whereas the 8th and 9th segments contain 30 slices. Figures 3(A) and (B) illustrate these frameworks for the nonTOF PET data to achieve direct AC in the sinogram domain and estimate the ACF matrices from nonAC sinograms, respectively. To generate the final PET sinograms or ACF matrices for PET image reconstruction, the resulting 9 different segments are simply concatenated to create standard sinograms or ACF matrices.

Similarly, the training of the TOF PET data can be carried out separately for each segment. Figures 4(A) and (B) illustrate direct AC in the sinogram domain and estimation of the ACF matrices from TOF PET data separately for each segment, respectively. Likewise, the final standard emission and ACF matrices are generated through concatenation of the resulting segments.

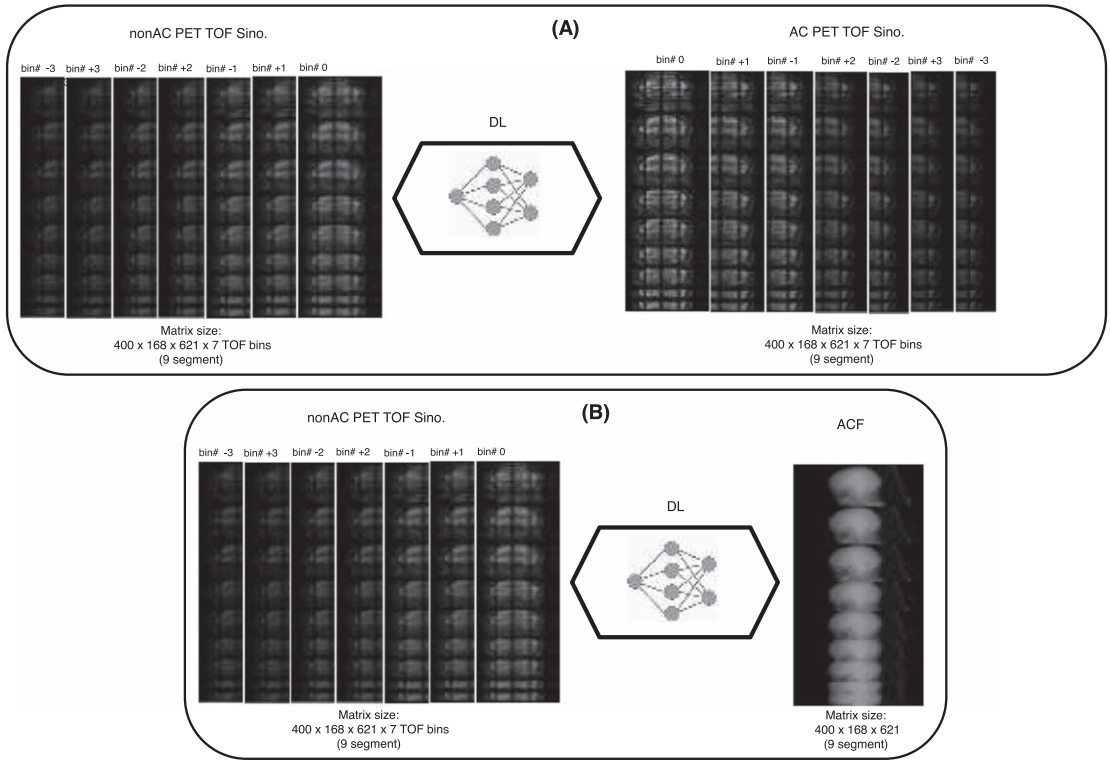

Figure 2. (A) Direct estimation of the attenuation corrected sinogram (AC Sino.) from nonAC TOF PET data and (B) Estimation of ACFs from TOF PET sinogram using all 9 segments.

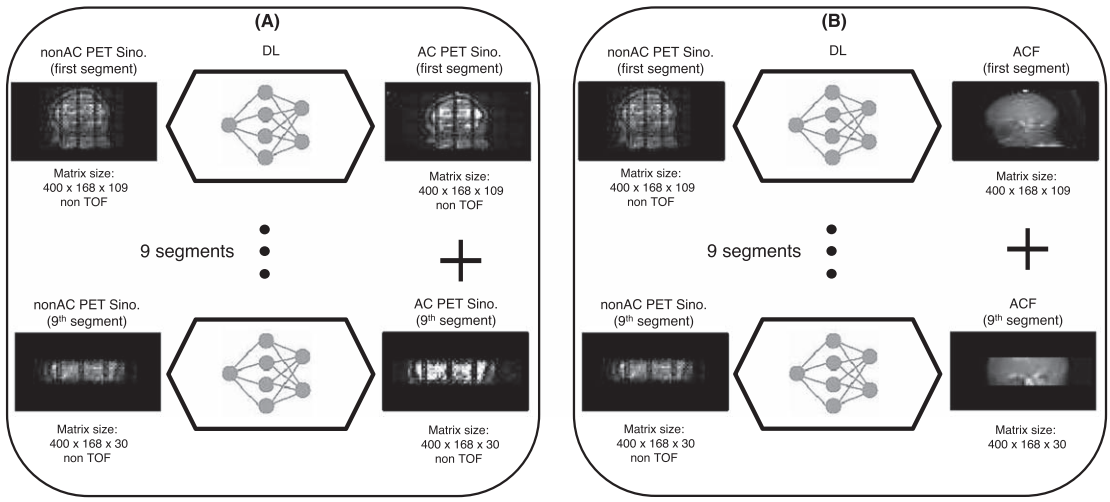

Figure 3. (A) Direct estimation of the attenuation corrected sinogram (AC Sino.) from nonAC nonTOF PET data and (B) estimation of ACFs from nonTOF PET sinogram separately for each segment.

2.2.4. Impact of scatter correction

The inputs to the deep learning models shown in figures 1–4 to estimate either AC emission sinograms or ACF matrices for both TOF or nonTOF PET data are the nonAC emission sinograms after normalization and random correction. As extensively discussed in our previous study (Arabi and Zaidi 2020), correction for scattered photons could also be applied prior to training the models. The impact of scatter correction could be investigated for the different AC strategies in the sinogram domain. A single scatter sinogram was estimated for each subject where nonAC sinograms (either TOF or nonTOF) were corrected prior to training of the models illustrated in figures 1 and 2. The models trained with and without prior scatter correction were compared to put into perspective the impact of scatter correction.

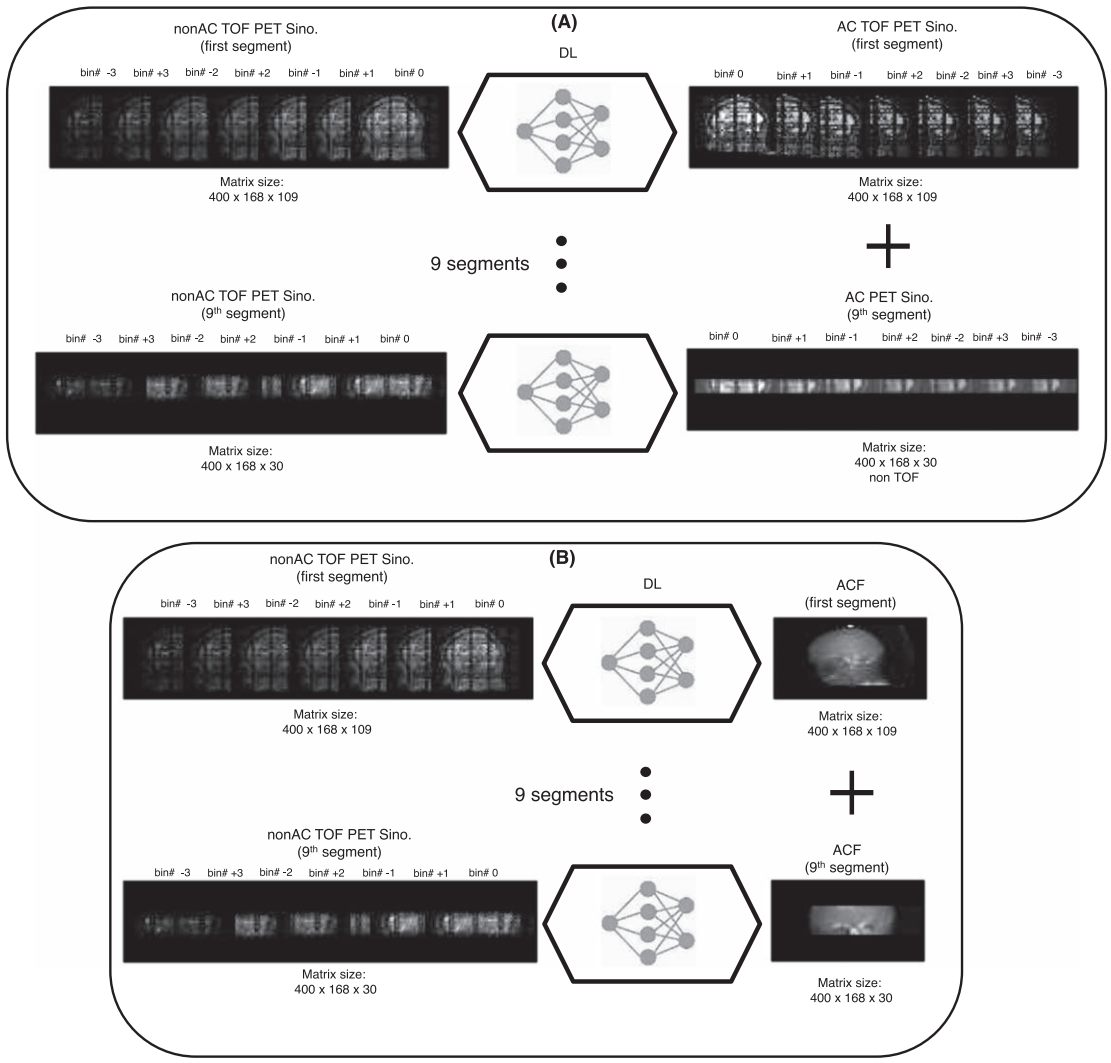

Figure 4. (A) Direct estimation of attenuation corrected sinogram (AC Sino.) from nonAC TOF PET data and (B) estimation of ACFs from TOF PET sinograms separately for each segment.

2.2.4.1. Estimation of the scatter sinogram

Scatter events may adversely affect the performance of AC approaches in the sinogram domain as demonstrated in our previous study (Arabi and Zaidi 2020). To take scattered events into account, the scatter sinograms were estimated from the segmented (background air and soft-tissue) AC map. To this end, nonAC TOF PET images were reconstructed for each subject based on which the head contour was differentiated from background air. To generate the segmented AC map, attenuation coefficients of water 0.1 cm^{-1} ($\approx$ 0 HU) and air 0.0 cm^{-1} (≈ -1000 HU) were assigned to voxels inside the head contour and the background air, respectively. Two-class AC maps were estimated from the segmentation of TOF reconstructed PET-nonAC images. TOF reconstruction of PET-nonAC images provides distinctive/strong signals to segment the head contour from background air (Burgos *et al* 2014). The head contour was automatically defined using a thresholding-based segmentation algorithm, followed by assignment of attenuation coefficients of 0.1 cm^{-1} (0 HU) and 0.0 cm^{-1} (-1000 HU) to voxels located within the head contour and background air, respectively. Given the 2-class AC maps, TOF PET image reconstruction was performed for all subjects using an ordinary Poisson ordered subsets-expectation maximization (OP-OSEM) algorithm implemented in the Siemens e7 tools with 4 iteration and 21 subsets. The resulting scatter sinograms are in the same dimensions as the nonTOF PET sinogram or ACF matrices (400 $\times$ 168 $\times$ 621 elements in 9 segments) for both TOF and nonTOF PET image reconstruction. The scatter sinograms obtained from these reconstructions were exploited to correct the nonAC sinograms (either TOF or nonTOF) prior to training the models as described in section 2.2.4. The single scatter simulation (SSS) algorithm (implemented in the Siemens e7 tool) was employed to estimate the scatter sinograms scaled by the tail fitting approach (Watson 2007). Previous studies demonstrated that the scatter sinograms estimated from a synthetic CT (for instance the 2-class AC map) are in close agreement with reference to CT-based scatter estimation (Burgos *et al* 2014, Arabi and Zaidi 2020). Therefore, the impact of scatter correction prior to training

Table 1. Summary of the different strategies for attenuation correction in the sinogram domain.

	Input	Output
nonTOF/D	nonTOF nonAC sinogram	nonTOF AC sinogram
TOF/D	TOF nonAC sinogram	TOF AC sinogram
nonTOF/A	nonTOF nonAC sinogram	ACF
TOF/A	TOF nonAC sinogram	ACF
nonTOF/D/Seg	nonTOF nonAC sinogram separately for each segment	nonTOF AC sinogram separately for each segment
TOF/D/Seg	TOF nonAC sinogram separately for each segment	TOF AC sinogram separately for each segment
nonTOF/A/Seg	nonTOF nonAC sinogram separately for each segment	ACF separately for each segment
TOF/A/Seg	TOF nonAC sinogram separately for each segment	ACF separately for each segment
nonTOF/D/Sca	nonTOF nonAC sinogram corrected for scatter	nonTOF AC sinogram
TOF/D/Sca	TOF nonAC sinogram corrected for scatter	TOF AC sinogram
nonTOF/A/Sca	nonTOF nonAC sinogram corrected for scatter	ACF
TOF/A/Sca	TOF nonAC sinogram corrected for scatter	ACF

the models was also investigated in this study motivated by the fact that generation of the 2-class AC maps and their corresponding scatter sinograms are practically feasible even for standalone PET scanners.

To summarize the strategies evaluated in this work, table 1 lists the different AC models in the sinogram domain with their corresponding input and output data for both TOF and nonTOF PET imaging.

2.3. Deep learning framework

The NiftyNet platform, an open-source code consisting of a number of deep learning modules for medical image analysis research (Gibson *et al* 2018), was adopted to implement the twelve strategies listed in table 1. Niftynet was built upon TensorFlow libraries in Python environment and configured in regression mode to predict AC sinograms or ACF matrices from nonAC sinograms. To this end, the HighResNet architecture (implemented on TensorFlow (version 1.12) in Phython environment (version 3.6)), consisting of 20 residual convolutional layers with varying dilation factors (Li *et al* 2017), was retrieved and modified (adjusting the input/output layers according to the sinogram matrix sizes and the number of input channels) to implement the models listed in table 1.

Prior to training the models, all PET emission sinograms (either TOF or nonTOF, AC on nonAC) were normalized by a predefined activity concentration to adjust the intensity values within the range [0–3]. To maintain the quantitative aspect of emission data, the AC and nonAC sinograms (for all datasets) were normalized by predefined activity of 19 MBq ($\approx$ 9 SUV) and 7 MBq ($\approx$ 3 SUV), respectively. For ACF sinograms, the inverse matrices were calculated to convert the intensity values to [0–1]. The training (and evaluation) of the models were carried out using the following hyperparameters as elaborated in (Arabi and Zaidi 2020): spatial window $= 168 \times 400$, batch size $= 10$, optimizer $=$ Adam, learning rate $= 0.005$ to 0.001 (following an optimization steps elaborated in Smith 2018), loss function $=$ L2norm, decay $= 0.0002$ and 0 (following an optimization steps elaborated in Smith 2018), and sample per subject $= 1$. The training of the models was performed plane-wise, wherein all emission and attenuation data for a single acquisition plane was regarded as a single training sample (two-dimensional). For TOF models, the information in the 7 TOF bins was fed into the deep learning networks with 7 input channels (TOF data in the different TOF bins were processed simultaneously). The models were implemented in an NVIDIA GEFORCE RTX 2080 Ti platform.

It should be noted that only 7 out of 13 TOF sinogram bins (-3 to $+3$) were used for the training and evaluation of the models in TOF imaging since the remaining 6 TOF sinogram bins bear almost no relevant information with respect to tracer uptake in the head region. Moreover, PET sinograms generated by the Biograph mCT scanner for either TOF or nonTOF imaging contain 621 direct and oblique planes for each bed acquisition. The training of all 12 models was carried out plane-wise wherein at each training or validation iteration single plane (either direct or oblique) with dimensions of 400×168 voxels for nonTOF and 7 (TOF bins) $\times$ 400×168 voxels for TOF models were considered as input/output of the networks. However, the training and evaluation of the models (TOF/A/Seg, nonTOF/A/Seg, TOF/D/Seg, and nonTOF/D/Seg) shown in figures 3 and 4 were performed separately for direct and obliques planes. In figures 1 and 2, all sinograms and ACF matrices, including direct or obliques planes are illustrated as input/ouput of the models. However, in practice, at each iteration a single row of the sinogram corresponding to a single plane (out of 621) was used as a single training sample.

The training of these 12 models was carried using 50 subjects whereas the evaluation was performed on 20 subjects. Five percent (5%) of the training dataset was used as the validation dataset within the training process for parameter optimization and verification of overfitting.

2.4. Evaluation strategy

The first part of the evaluation involved estimation of the standardized uptake value (SUV) bias within the major tissue types, including bone, air cavities, and soft-tissue. Conventional CT-based attenuation and scatter correction of PET data was considered as reference for all comparisons throughout the manuscript. To this end, CT images were segmented using an intensity threshold level of >150 HU for bony structures, <−400 HU for air cavities within the head contour and between −400 HU and 150 HU for soft-tissue. Considering PET-CT images as reference, SUV bias in terms of mean relative error and mean relative absolute error was estimated for the different models listed in table 1 using equations (1) and (2), respectively

$$\mathrm{RE}\ (\%) = \frac{1}{V}\sum_{v=1}^{V}\left(100 \times \frac{\mathrm{PET_{DL}}(v) - \mathrm{PET_{CT}}(v)}{\mathrm{PET_{CT}}(v)}\right), \tag{1}$$

$$\mathrm{RAE}(\%) = \frac{1}{V}\sum_{v=1}^{V}\left|100 \times \frac{\mathrm{PET_{DL}}(v) - \mathrm{PET_{ct}}(v)}{\mathrm{PET_{CT}}(v)}\right|. \tag{2}$$

Here, V stands for the total number of voxels within the head region or any of the major tissue types, $\mathrm{PET_{CT}}(v)$ and $\mathrm{PET_{DL}}(v)$ indicate the SUV of voxel v within the reference PET-CT and PET images obtained from one of the models listed in table 1. In addition to these models, the segmented AC map employed for the generation of the scatter sinogram was included in the comparative evaluation, which represents the AC map generation method implemented on the Philips TF PET/MRI scanner (Zaidi *et al* 2011). PET image reconstruction was performed using an iterative ordinary Poisson ordered subsets-expectation maximization (OP-OSEM) algorithm (4 iteration and 21 subsets) and post-reconstruction Gaussian smoothing with a 2 mm FWHM.

Moreover, peak signal-to-noise ratio (PSNR), structural similarity index (SSIM), and root mean square error (RMSE) were computed between the reference PET-CT and different AC models for the head region using equations (3)–(5), respectively

$$\mathrm{PSNR(dB)} = 10\log_{10}\left(\frac{\mathrm{MaxVal}^2}{\mathrm{MSE}}\right), \tag{3}$$

$$\mathrm{SSIM} = \frac{(2 \times \mathrm{mean}\ (\mathrm{PET_{CT}}) \times \mathrm{mean}\ (\mathrm{PET_{DL}}) + C_1)(2\delta_{\mathrm{PET_{CT},PETDL}} + C_2)}{(\mathrm{mean}\ (\mathrm{PET_{CT}})^2 + \mathrm{mean}\ (\mathrm{PET_{DL}})^2 + C_1)(\delta^2_{\mathrm{PETCT}} + \delta^2_{\mathrm{PETDL}} + C_2)}, \tag{4}$$

$$\mathrm{RMSE} = \sqrt{\frac{1}{V}\sum_{v=1}^{V}(\mathrm{PET_{DL}}(v) - \mathrm{PET_{CT}}(v))^2}. \tag{5}$$

MaxVal in equation (3) stands for the maximum intensity value of either $\mathrm{PET_{CT}}$ or $\mathrm{PET_{DL}}$ images whereas MSE denotes the mean squared error. In equation (4), mean(PET) returns the mean value of the PET image while variances of $\mathrm{PET_{CT}}$ and $\mathrm{PET_{tst}}$ images are denoted by δ_{PETCT} and δ_{PETDL}, respectively, and $\delta_{\mathrm{PETCT,PETDL}}$ indicates their covariance. $C_1 = 0.01$ and $C_2 = 0.02$ are constant variables used to avoid division by very small values or zero.

The quantitative evaluation of PET images was extended to calculate the SUV bias in 63 brain regions using the Hermes BRASS tool for brain analysis (Hermes Medical Solutions AB, Sweden). This tool provides standard templates for PET and MR brain images to map the patient/test PET images into a common/standard spatial coordinate. The relative SUV bias (SB(%)) and absolute relative SUV bias (ASB(%)) were estimated for the different brain regions using equations (6) and (7), respectively, wherein the brain regions are indicated by R

$$\mathrm{SB}(\%) = \frac{(\mathrm{PET_{DL}})_R - (\mathrm{PET_{CT}})_R}{(\mathrm{PET_{CT}})_R} \times 100\%, \tag{6}$$

$$\mathrm{ASB}(\%) = \left|\frac{(\mathrm{PET_{DL}})_R - (\mathrm{PET_{CT}})_R}{(\mathrm{PET_{CT}})_R}\right| \times 100\%. \tag{7}$$

In addition, joint histogram analysis was performed to display the voxel-wise correlations between activity concentration in reference PET-CT and the different PET images. Paired t-test analysis was employed to assess the statistical significance of the difference between results obtained from the different models considering a p-value <0.05 as a statistically valid difference.

3. Results

The quantitative evaluation of PET images resulting from the different AC models listed in table 1 along with the 2-class AC map are reported in supplemental table 1 (available online at stacks.iop.org/PMB/66/145001/mmedia) and figure 5 for the head region as well as within bone, soft-tissue, and air cavities. Table 2 also compares the different models along with the 2-class AC map in terms of PSNR, RMSE, and SSIM for the head region. Overall, TOF models outperformed as expected nonTOF models and the 2-class AC map. In this regard,

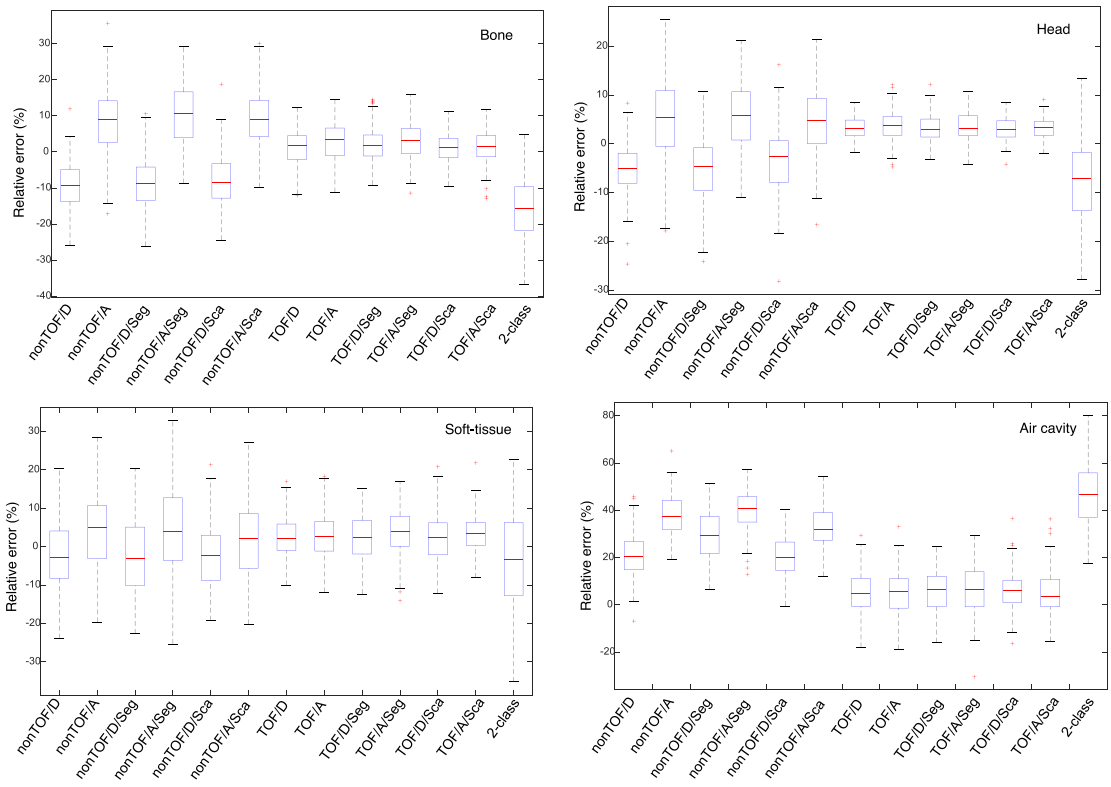

Figure 5. Relative errors (%) of PET images resulting from the different AC strategies in the sinogram domain along with the 2-class AC map within the head region, bony structures, air cavity, and soft-tissue.

Table 2. RMSE (SUV), SSIM, and PSNR (dB) calculated for the different AC strategies in the sinogram domain along with the 2-class AC map within the whole head region.

	RMSE (SUV)	PSNR (dB)	SSIM
nonTOF/D	0.6 ± 0.02	31.9 ± 1.2	0.92 ± 0.02
nonTOF/A	0.7 ± 0.02	31.3 ± 1.2	0.91 ± 0.02
nonTOF/D/Seg	0.7 ± 0.02	31.4 ± 1.2	0.91 ± 0.02
nonTOF/A/Seg	0.7 ± 0.02	31.0 ± 1.2	0.91 ± 0.02
nonTOF/D/Sca	0.6 ± 0.02	32.0 ± 1.2	0.92 ± 0.02
nonTOF/A/Sca	0.7 ± 0.02	31.6 ± 1.2	0.91 ± 0.02
TOF/D	0.3 ± 0.02	33.5 ± 1.6	**0.93 ± 0.02**
TOF/A	0.5 ± 0.03	32.2 ± 1.3	0.92 ± 0.02
TOF/D/Seg	0.4 ± 0.02	33.0 ± 1.6	0.92 ± 0.02
TOF/A/Seg	0.5 ± 0.04	32.1 ± 1.3	0.92 ± 0.02
TOF/D/Sca	**0.3 ± 0.01**	33.7 ± 1.6	**0.93 ± 0.02**
TOF/A/Sca	**0.3 ± 0.01**	**33.8 ± 1.5**	**0.93 ± 0.02**
2-class	0.9 ± 0.02	30.5 ± 1.1	0.89 ± 0.03

nonTOF models, in particular nonTOF/D (figure 1(A)) and nonTOF/D/Sca, exhibited superior performance over the 2-class AC map. The *p*-values reported in tables 3 and 4 confirm that the differences between TOF and nonTOF models as well as the 2-class AC map were statistically significant. Moreover, the separation of the sinogram segments deteriorated the performance of both TOF and nonTOF models. The *p*-values reported in tables 3 and 4 substantiate that separate training of each sinogram segment as illustrated in figure 3 would lead to sub-optimal outcomes.

Considering only nonTOF strategies, nonTOF/D and nonTOF/D/Sca exhibited overall better performance compared to the other nonTOF models. The differences between these two models were not statistically significant, indicating the insensitivity of direct nonAC to AC sinogram conversion (figure 1(A)) to prior scatter correction. Estimation of the ACF matrices from nonTOF sinograms, nonTOF/A and nonTOF/A/Sca models, showed sub-optimal results compared to nonTOF/D and nonTOF/D/Sca models.

Table 3. P-values calculated among the AC models along with the 2-class AC map for the results reported in supplemental table 1 and figure 5.

p-value	Soft-tissue	Bone	Air cavity	Head
nonTOF/D versus nonTOF/D/Sca	0.1	0.08	0.06	0.09
nonTOF/D versus nonTOF/A/Sca	0.05	<0.05	<0.02	<0.05
nonTOF/D versus nonTOF/D/Seg	0.05	<0.05	<0.05	<0.05
nonTOF/D versus 2-class	<0.05	<0.01	<0.01	<0.02
TOF/D versus TOF/D/Sca	0.08	0.05	0.06	0.08
TOF/D/Sca versus TOF/A/Sca	0.08	0.06	0.07	0.08
TOF/A/Sca versus TOF/A	<0.05	<0.05	<0.02	<0.05
TOF/D/Sca versus TOF/D/Seg	0.05	<0.05	<0.05	0.05
TOF/A/Sca versus 2-class	<0.02	<0.01	<0.01	<0.01
TOF/A/Sca versus nonTOF/D	<0.05	<0.01	<0.01	<0.02
TOF/A/Sca versus nonTOF/D/Sca	<0.05	<0.02	<0.02	<0.02

Table 4. *P*-values calculated among the AC models along with the 2-class AC map for the results reported in table 2.

p-value	RMSE	PSNR	SSIM
nonTOF/D versus nonTOF/D/Sca	0.08	0.09	0.11
nonTOF/D versus nonTOF/A/Sca	<0.05	0.05	0.05
nonTOF/D versus nonTOF/D/Seg	<0.05	<0.05	<0.05
nonTOF/D versus 2-class	<0.05	<0.05	<0.05
TOF/D versus TOF/D/Sca	0.05	0.06	0.06
TOF/D/Sca versus TOF/A/Sca	0.08	0.09	0.10
TOF/A/Sca versus TOF/A	<0.05	<0.05	<0.05
TOF/D/Sca versus TOF/D/Seg	<0.05	<0.05	0.05
TOF/A/Sca versus 2-class	<0.01	<0.01	<0.01
TOF/A/Sca versus nonTOF/D	<0.01	<0.01	<0.01
TOF/A/Sca versus nonTOF/D/Sca	<0.01	<0.01	<0.02

Among TOF strategies, TOF/A/Sca, TOF/D, and TOF/D/Sca models resulted in significantly less quantitative errors compared to the other models. Similar to nonTOF/D and nonTOF/D/Sca models, the correction for scattered photons prior to training the TOF/D model did not significantly impact the its outcome. However, correction for scatter in TOF/A/Sca seems to be critical as TOF/A models achieved lower performance compared to TOF/D and TOF/A/Sca models. Similar to nonTOF models, separation of the sinogram segments had an adverse impact on the training of the TOF models, leading to sub-optimal performance.

Among nonTOF AC strategies, nonTOF/D and nonTOF/D/Sca models, and among the TOF AC strategies, TOF/D and TOF/A/Sca models showed relatively higher accuracy. Hence, in the following, the results associated with these models along with the 2-class AC maps are presented. The quantitative accuracy of the radiotracer uptake in the different brain regions was evaluated for nonTOF/D, nonTOF/D/Sca, TOF/D, TOF/A/Sca models, and the 2-class AC map through mapping the resulting PET images to the BRASS brain PET template. The BRASS template provides 63 distinct brain regions with left and right compartments. The mean SUV bias (SB% and ASB%) are reported for the 20 largest brain regions averaged over the left and right compartments in table 5 and Supplemental figure 1. The differences between TOF and nonTOF models, nonTOF models and the 2-class AC map as well as TOF models and the 2-class AC map were statistically significant (p-values<0.04). However, there was no proof of statistically significant differences between nonTOF/D and nonTOF/Sca and also TOF/D and TOF/A/Sca. Moreover, the SUV bias maps calculated over PET images of 20 test patients (after mapping to the BRASS template) are displayed in figure 6 for the different AC models.

The results of the joint histogram analysis and the plot of the voxel-wise correlation between the radiotracer uptake in PET images resulting from the different AC models and reference PET-CT images are presented in figure 7. The linear regression analysis carried out on the 20 test patients exhibited a high correlation for TOF/D and TOF/A/Sca models ($R^2 = 0.99$) while nonTOF/D and nonTOF/D/Sca resulted in $R^2 = 0.985$ while the 2-class AC map achieved $R^2 = 0.981$.

Table 5. Mean relative (SB) and absolute relative (ASB) SUV bias calculated in 20 brain regions for the different AC strategies in the sinogram domain along with the 2-class AC map.

	TOF/D **SB ± std (ASB ± std)**	TOF/A/Sca **SB ± std (ASB ± std)**	nonTOF/D **SB ± std (ASB ± std)**	nonTOF/D/Sca **SB ± std (ASB ± std)**	2-class **SB ± std (ASB ± std)**
Cerebellum	**2.3 ± 4.5** (**5.6 ± 3.9**)	2.4 ± 4.6 (5.7 ± 4.0)	−5.7 ± 5.9 (7.3 ± 4.9)	−5.5 ± 5.7 (7.1 ± 4.8)	−8.9 ± 5.6 (10.3 ± 4.7)
Gyros (G.) frontalis	**3.4 ± 4.2** (**5.8 ± 3.6**)	0.9 ± 5.3 (6.0 ± 4.2)	−5.9 ± 5.6 (8.0 ± 4.9)	−6.2 ± 5.8 (8.3 ± 5.0)	−9.2 ± 6.1 (12.3 ± 5.2)
G.front.sup.pars med.	**2.2 ± 4.2** (**5.8 ± 3.0**)	4.8 ± 3.9 (5.9 ± 3.1)	4.3 ± 5.3 (6.5 ± 4.9)	1.0 ± 5.7 (6.9 ± 4.6)	−6.8 ± 6.1 (9.2 ± 5.1)
G.precentralis	4.4 ± 3.9 (6.0 ± 3.4)	**−0.5 ± 5.5** (**5.3 ± 4.6**)	0.5 ± 5.1 (5.6 ± 4.0)	−3.8 ± 3.8 (5.8 ± 3.2)	−3.1 ± 7.4 (8.6 ± 5.5)
Lobulus paracentralis	**0.4 ± 4.9** (**5.1 ± 4.0**)	4.8 ± 2.9 (5.7 ± 2.3)	2.1 ± 4.8 (5.7 ± 4.0)	5.8 ± 3.7 (6.1 ± 3.5)	−7.8 ± 5.9 (11.3 ± 4.8)
G.rectus	**3.8 ± 4.6** (**4.9 ± 3.9**)	−0.1 ± 5.7 (5.1 ± 4.2)	4.1 ± 3.6 (5.1 ± 3.0)	1.2 ± 4.9 (5.6 ± 4.1)	−10.8 ± 6.3 (13.9 ± 5.0)
G.orbitalis	1.2 ± 4.8 (5.0 ± 3.4)	5.1 ± 3.4 (5.5 ± 2.9)	**0.1 ± 4.3** (**3.9 ± 3.2**)	−2.3 ± 3.9 (4.1 ± 3.0)	−7.3 ± 5.9 (8.7 ± 4.8)
G.temporalis	**−1.9 ± 5.6** (**3.9 ± 3.8**)	−5.9 ± 4.4 (4.1 ± 3.0)	4.7 ± 3.7 (5.0 ± 3.0)	0.7 ± 5.1 (4.3 ± 2.9)	−11.3 ± 7.9 (14.0 ± 6.3)
G.postcentralis	2.2 ± 4.9 (5.7 ± 3.7)	**−3.8 ± 4.1** (**4.9 ± 3.4**)	5.1 ± 4.4 (6.5 ± 3.9)	4.4 ± 4.3 (6.0 ± 3.5)	−4.9 ± 6.9 (7.6 ± 6.0)
Lobulus par.inf.	**−1.1 ± 5.4** (**5.8 ± 4.7**)	5.1 ± 4.6 (6.5 ± 4.0)	−6.1 ± 4.0 (6.9 ± 3.8)	−4.1 ± 4.5 (6.0 ± 3.9)	2.3 ± 7.4 (6.5 ± 5.9)
G.supramarginalis	**2.9 ± 4.7** (**5.7 ± 4.0**)	−2.1 ± 5.1 (5.9 ± 4.3)	−5.8 ± 4.9 (8.2 ± 4.3)	−6.7 ± 5.3 (9.5 ± 4.2)	−1.9 ± 6.9 (5.8 ± 6.0)
G.angularis	**2.8 ± 4.7** (**5.5 ± 3.9**)	0.9 ± 5.0 (5.9 ± 4.1)	−4.1 ± 3.9 (6.9 ± 3.5)	−6.5 ± 5.3 (9.1 ± 4.7)	1.8 ± 7.0 (6.0 ± 5.9)
Lobulus par.sup.	5.3 ± 4.3 (6.5 ± 3.9)	**4.0 ± 4.1** (**5.4 ± 3.4**)	−1.3 ± 4.4 (5.8 ± 4.2)	2.2 ± 5.4 (6.3 ± 4.6)	−3.7 ± 6.2 (9.8 ± 5.2)
G.occipitalis	−1.7 ± 4.9 (4.7 ± 4.0)	**1.6 ± 4.5** (**4.0 ± 3.7**)	2.3 ± 5.1 (6.5 ± 4.5)	−4.9 ± 3.9 (5.4 ± 3.4)	−9.9 ± 7.3 (13.1 ± 5.6)
Cuneus	**2.6 ± 4.4** (**4.8 ± 3.9**)	−1.5 ± 5.0 (5.0 ± 4.1)	−5.8 ± 4.7 (8.3 ± 4.1)	−6.7 ± 5.0 (9.1 ± 4.1)	−8.1 ± 6.3 (11.1 ± 5.2)
Precuneus	**4.2 ± 4.6** (**5.4 ± 3.9**)	−0.5 ± 5.5 (6.1 ± 4.3)	−0.8 ± 5.0 (6.2 ± 4.0)	2.9 ± 4.8 (7.1 ± 3.9)	2.4 ± 7.3 (1.8 ± 5.9)
Putamen	0.3 ± 4.8 (5.2 ± 4.1)	**3.3 ± 4.4** (**5.0 ± 3.6**)	−7.0 ± 4.9 (9.2 ± 3.1)	−4.5 ± 4.5 (8.0 ± 3.9)	−7.8 ± 4.7 (12.8 ± 3.0)
Hippocampus	**−4.1 ± 4.3** (**5.0 ± 3.6**)	−0.3 ± 4.7 (5.2 ± 3.8)	−0.2 ± 5.0 (6.6 ± 4.3)	1.8 ± 5.6 (7.3 ± 4.5)	2.4 ± 7.9 (8.6 ± 5.5)
G.occipitotemp	**2.1 ± 5.8** (**5.6 ± 4.3**)	5.0 ± 5.4 (6.1 ± 4.2)	1.5 ± 5.5 (8.1 ± 4.7)	−1.1 ± 5.6 (7.3 ± 4.9)	−10.3 ± 7.6 (13.9 ± 4.9)
Thalamus	**3.2 ± 4.7** (**4.8 ± 4.0**)	4.1 ± 4.7 (5.3 ± 4.0)	−1.8 ± 4.6 (7.4 ± 3.8)	−6.9 ± 4.8 (9.1 ± 3.9)	−10.0 ± 7.5 (13.0 ± 4.7)

4. Discussion

The primary motivation to estimate ACFs or perform attenuation correction in the sinogram domain is that the PET data bear object-specific information regarding the attenuation medium within the FOV as demonstrated in our previous study (Arabi and Zaidi 2020). Due to the extended data representation in the sinogram domain, a wider spectrum of strategies can be adopted to estimate ACF matrices or to directly apply attenuation and scatter correction in this domain (Zaidi and El Naqa 2021). This study focussed on the implementation and comparison of different AC strategies in the sinogram space for both TOF and nonTOF PET data to determine the most accurate and appealing approaches.

Overall, TOF models outperformed nonTOF models as well as the 2-class segmentation-based approach. This can be explained by the fact that the different TOF bins belonging to the same acquisition plane convey exactly the same information regarding the attenuation medium across the acquisition plane, though the activity distributions vary (Surti 2015). The inclusion of TOF data increases the number of samples from each acquisition plane, thus resulting in a more accurate ACF estimation or a correction for attenuated and scattered photons. In comparison to nonTOF models, the number of samples from each PET acquisition plane in TOF models increased by a factor of 7 (7 significant TOF bins out of 13), which led to a more accurate extraction of the

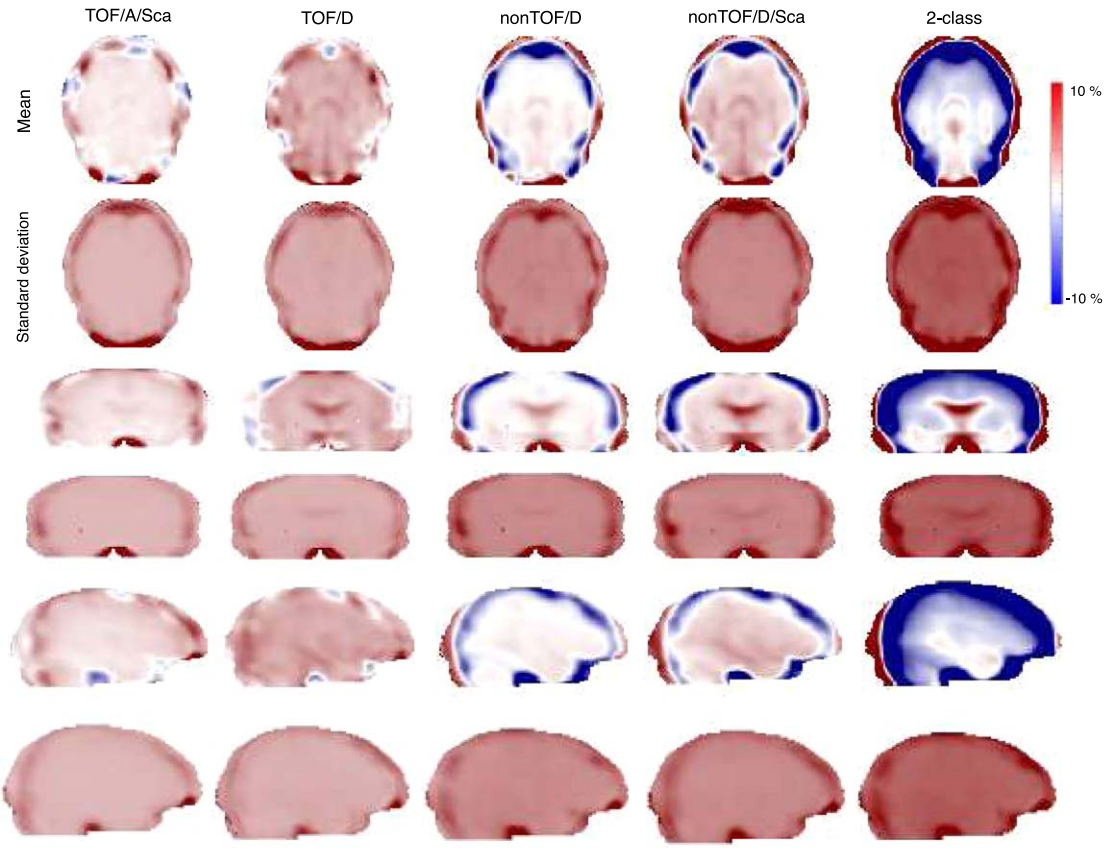

Figure 6. Transaxial, coronal, and sagittal views of SUV bias maps representing the mean and standard deviation calculated over 20 patients using the BRASS template for the different AC models.

latent information regarding the attenuated photons and/or attenuating medium from the emission data. Though nonTOF models (in particular nonTOF/D and nonfTOF/D/Sca) exhibited sub-optimal performance compared to TOF models, these models largely outperformed the 2-class segmentation-based approach, which was included in this study to provide a base for comparison with other studies and magnitude of expected SUV bias in clinical setting.

Depending on the axial coverage of PET acquisition and/or axial acceptance angle, PET sinograms come in a number of segments (for the mCT scanner with an extended axial FOV, the number of segments is 9) viewing the activity distribution from different angles. Separate training of the models, either nonTOF or TOF, for the different segments of the sinograms (figures 3 and 4) led to sub-optimal outcomes. A plausible justification for this observation is that the different segments of the sinogram convey highly correlated information about both activity distribution and attenuating medium, though they are acquired at different angles. Hence, combining these segments within the training process enabled faster convergence of these models owing to the increased number of samples from a single input subject. Separate training of the models for each sinogram segment reduced the number of training samples by nine (number of segments).

Regarding the nonTOF models, direct estimation of the AC sinogram (nonTOF/D) showed no significant sensitivity to prior scatter correction as the differences between nonTOF/D and nonTOF/D/Sca models were not statistically significant. This demonstrates that the deep learning model can effectively detect and correct/remove scattered counts from nonAC sinogram to estimate AC emission sinograms. However, prior scatter correction for estimation of the ACF matrices was critical since significant differences were observed between nonTOF/A and nonTOF/A/Sca models. Overall, among nonTOF models, nonTOF/D would be the method of choice since it requires no prior correction for scattered photons, requires only a single input/output channel, and exhibited superior performance over the 2-class segmentation-based method.

A similar observation was made for TOF models wherein direct estimation of the AC sinogram from PET-nonAC emission data (TOF/D and TOF/D/Sca models) showed almost no sensitivity to prior correction for scattered photons. Therefore, TOF/D method could be an efficient approach as it achieved significantly less quantitative bias compared to the 2-class AC map as well as nonTOF/D model. However, TOF/D models requires input/output channels equal to the number of TOF bins which might be an important limitation for PET scanners with high TOF coincidence time resolution (up to 23 TOF bins for 214 ps resolution on the

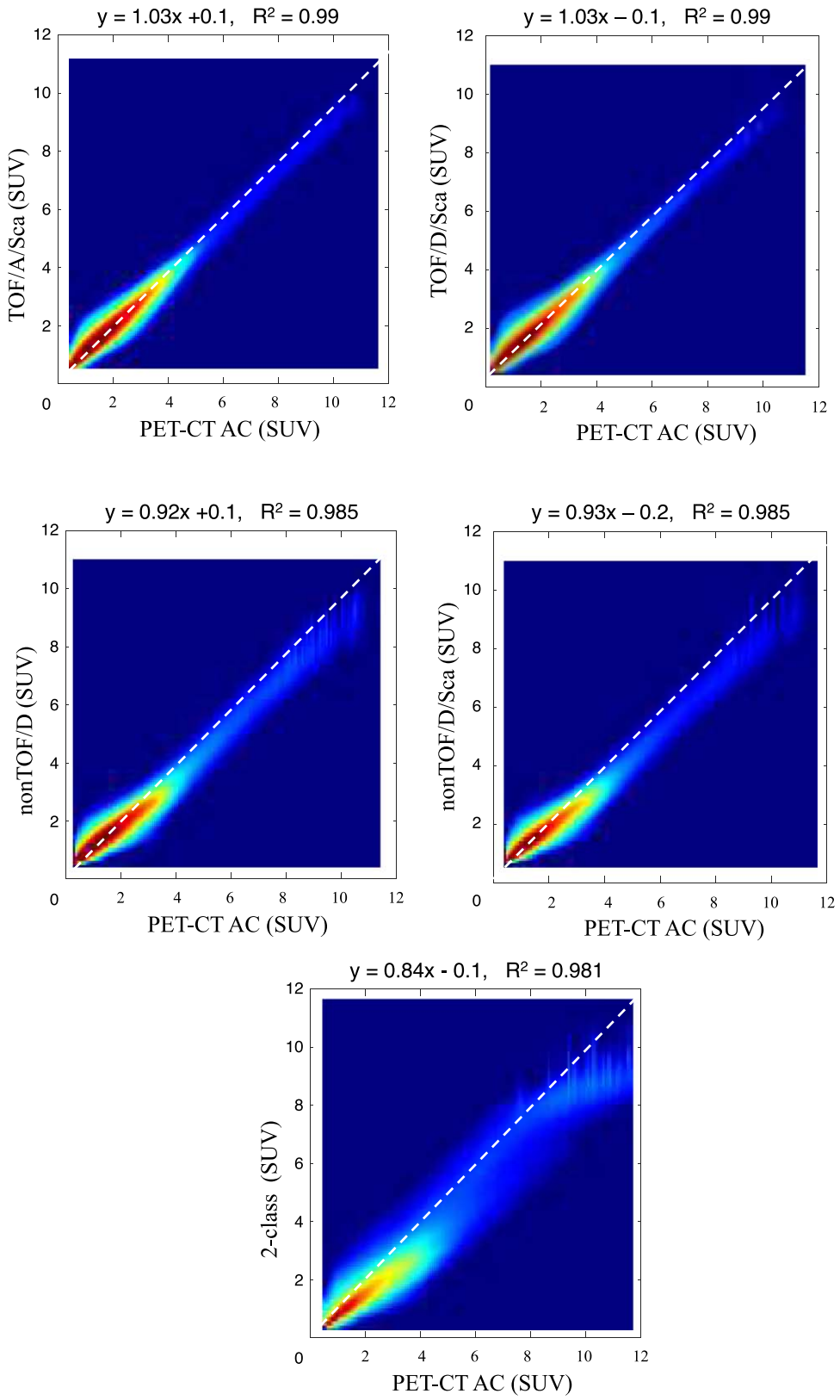

Figure 7. Joint histograms of voxel-wise SUV for the different PET AC models versus reference PET/CT images.

Siemens Biograph Vision PET/CT scanner van Sluis *et al* 2020). TOF/A/Sca model, which predicts the ACFs from the PET emission data, exhibited similar performance to the TOF/D model and could be the method of choice for TOF PET imaging. The advantage of this method is that regardless of the TOF resolution (number of TOF bins), it requires only a single output channel. However, to reach peak performance, this model requires

prior estimation of scattered photons from a synthetic attenuation map (such as the 2-class AC map), which complicates the implementation and application of this model.

The main findings of this work are two-fold. First, the performance differences between TOF and nonTOF models indicate the beneficial impact of TOF information to resolve the correlation between emission and attenuation data (table 5). These differences would be more appreciable if emission data with improved TOF resolution are investigated. Second, the contribution of prior scatter correction for the ACF estimation and direct models is emphasized. Though prior scatter correction improved the performance of the ACF estimation models, the insensitivity of direct models (TOF/D and nonTOF/D) to prior scatter correction is considered as a major advantage of these models.

PET attenuation and scatter correction in the sinogram domain has the merit of being patient-specific (to some extent) without the need for anatomical imaging. These approaches could be exploited in dedicated organ-specific (brain or breast) PET scanners. Though low-dose CT and MRI-guided AC approaches are well-established in brain PET/CT and PET/MR imaging, respectively, sinogram-based AC methods could be exploited as complementary or quality control approaches since these methods are immune/insensitive to potential artifacts and motion in anatomical images. The use of different radiotracers might affect the performance/outcome of these models owing to different uptake patterns and/or signal-to-noise ratio. In this regard, the performance/outcome of sinogram models would be greatly dependent on the injected dose, noise levels, and signal-to-noise ratio. Higher injected activity would lead to stronger signals or improved signal-to-noise ratio to resolve the correction between emission and attenuation data. Therefore, the performance assessment of these models for different PET radiotracers and in low-dose imaging situations warrants further investigation.

The efficiency of the TOF models would depend on the number of TOF bins (TOF resolution) since improved TOF resolution provides localized and more specific information about the correlation between attenuation and emission data. However, whole-body imaging or improved TOF resolution (for instance 23 TOF bins on the Siemens Biograph Vision PET/CT scanner) requires many parallel input channels and heavy computational complexity. Owing to the independent correlation between attenuation and emission data for each plane, all models were implemented in 2D mode. Nevertheless, 3D implementation of such models would also benefit from inter-plane correlations and consistency of emission and attenuation data across the planes, hence leading to improved outcomes. In this light, 3D implementation of sinogram models along with multiple input channels for TOF PET data calls for the development of dedicated networks with efficient memory management and computational capacity to extract the latent information from TOF PET data.

5. Conclusion

This work set out to implement and investigate various deep learning-based strategies for PET attenuation correction in the sinogram domain. The models relying on TOF information significantly outperformed nonTOF models as well as segmentation-based 2-class AC map. Nevertheless, nonTOF models exhibited superior performance to the 2-class AC map. Estimation of the ACFs from PET emission data, either for TOF or nonTOF models, showed high sensitivity to prior scatter correction, while direct estimation of AC emission sinograms from nonAC sinograms revealed no sensitivity to scatter correction, thus obviating the need for prior scatter estimation. In this light, for nonTOF emission data, direct prediction of AC sinograms from non-attenuated corrected sinograms would be the method of choice. For TOF PET data, though direct prediction of the AC sinograms obviates the need for prior estimation of scattered photons, it requires input/output channels equal to the number of TOF bins. Prediction of ACF matrices from TOF PET data is less memory demanding as it requires only a single channel for output.

Acknowledgments

This work was supported by the Swiss National Science Foundation under grant SNRF 320030_176052, the Eurostars programme of the European commission under grant E! 114021 ProVision and the Private Foundation of Geneva University Hospitals under Grant RC-06-01.

Conflict of interest statement

The authors declare that they have no conflict of interest.

ORCID iDs

Habib Zaidi https://orcid.org/0000-0001-7559-5297

References

Arabi H, Bortolin K, Ginovart N, Garibotto V and Zaidi H 2020 Deep learning-guided joint attenuation and scatter correction in multitracer neuroimaging studies *Hum. Brain Mapp.* **41** 3667–79

Arabi H, Dowling J A, Burgos N, Han X, Greer P B, Koutsouvelis N and Zaidi H 2018 Comparative study of algorithms for synthetic CT generation from MRI: consequences for MRI-guided radiation planning in the pelvic region *Med. Phys.* **45** 5218–33

Arabi H, Koutsouvelis N, Rouzaud M, Miralbell R and Zaidi H 2016 Atlas-guided generation of pseudo-CT images for MRI-only and hybrid PET–MRI-guided radiotherapy treatment planning *Phys. Med. Biol.* **61** 6531

Arabi H, Rager O, Alem A, Varoquaux A, Becker M and Zaidi H 2015 Clinical assessment of MR-guided 3-class and 4-class attenuation correction in PET/MR *Mol. Imaging Biol.* **17** 264–76

Arabi H and Zaidi H 2016 One registration multi-atlas-based pseudo-CT generation for attenuation correction in PET/MRI *Eur. J. Nucl. Med. Mol. Imaging* **43** 2021–35

Arabi H and Zaidi H 2017 Comparison of atlas-based techniques for whole-body bone segmentation *Med. Image Anal.* **36** 98–112

Arabi H and Zaidi H 2020 Deep learning-guided estimation of attenuation correction factors from time-of-flight PET emission data *Med. Image Anal.* **64** 101718

Arabi H, Zeng G, Zheng G and Zaidi H 2019 Novel adversarial semantic structure deep learning for MRI-guided attenuation correction in brain PET/MRI *Eur. J. Nucl. Med. Mol. Imaging* **46** 2746–59

Bahrami A, Karimian A, Fatemizadeh E, Arabi H and Zaidi H 2020 A new deep convolutional neural network design with efficient learning capability: Application to CT image synthesis from MRI *Med. Phys.* **47** 5158–71

Baran J, Chen Z, Sforazzini F, Ferris N, Jamadar S, Schmitt B, Faul D, Shah N J, Cholewa M and Egan G F 2018 Accurate hybrid template-based and MR-based attenuation correction using UTE images for simultaneous PET/MR brain imaging applications *BMC Med. Imaging* **18** 41

Burgos N, Thielemans K, Cardoso M J, Markiewicz P, Jiao J, Dickson J, Duncan J S, Atkinson D, Arridge S R and Hutton B F 2014 *IEEE Nuclear Science Symp. and Medical Imaging Conf. (NSS/MIC), 2014* (Piscataway, NJ: IEEE) pp 1–5

Defrise M, Rezaei A and Nuyts J 2012 Time-of-flight PET data determine the attenuation sinogram up to a constant *Phys. Med. Biol.* **57** 885–99

Dinkla A M, Wolterink J M, Maspero M, Savenije M H F, Verhoeff J J C, Seravalli E, Isgum I, Seevinck P R and van den Berg C A T 2018 MR-only brain radiation therapy: Dosimetric evaluation of synthetic CTs generated by a dilated convolutional neural network *Int. J. Radiat. Oncol. Biol. Phys.* **102** 801–12

Emami H, Dong M, Nejad-Davarani S P and Glide-Hurst C 2018 Generating synthetic CT s from magnetic resonance images using generative adversarial networks *Med. Phys.* **45** 3627–36

Gibson E *et al* 2018 NiftyNet: a deep-learning platform for medical imaging *Comput. Methods Programs Biomed.* **158** 113–22

Gong K, Yang J, Kim K, El Fakhri G, Seo Y and Li Q 2018 Attenuation correction for brain PET imaging using deep neural network based on Dixon and ZTE MR images *Phys. Med. Biol.* **63** 125011

Han X 2017 MR-based synthetic CT generation using a deep convolutional neural network method *Med. Phys.* **44** 1408–19

Ladefoged C N *et al* 2017 A multi-centre evaluation of eleven clinically feasible brain PET/MRI attenuation correction techniques using a large cohort of patients *Neuroimage* **147** 346–59

Lee J S 2020 A review of deep-learning-based approaches for attenuation correction in positron emission tomography *IEEE Trans. Radiat. Plasma Med. Sci.* **5** 160–84

Leynes A P, Yang J, Shanbhag D D, Kaushik S S, Seo Y, Hope T A, Wiesinger F and Larson P E 2017 Hybrid ZTE/Dixon MR-based attenuation correction for quantitative uptake estimation of pelvic lesions in PET/MRI *Med. Phys.* **44** 902–13

Leynes A P, Yang J, Wiesinger F, Kaushik S S, Shanbhag D D, Seo Y, Hope T A and Larson P E Z 2018 Zero-echo-time and Dixon deep pseudo-CT (ZeDD CT): direct generation of pseudo-CT images for pelvic PET/MRI attenuation correction using deep convolutional neural networks with multiparametric MRI *J. Nucl. Med.* **59** 852–8

Li W, Wang G, Fidon L, Ourselin S, Cardoso M J and Vercauteren T 2017 *Int. Conf. Information Processing in Medical Imaging* (Berlin: Springer) pp 348–60

Liu F, Jang H, Kijowski R, Bradshaw T and McMillan A B 2018a Deep learning MR imaging-based attenuation correction for PET/MR imaging *Radiology* **286** 676–84

Liu F, Jang H, Kijowski R, Zhao G, Bradshaw T and McMillan A B 2018b A deep learning approach for 18 F-FDG PET attenuation correction *EJNMMI Phys.* **5** 24

Martinez-Moller A, Souvatzoglou M, Delso G, Bundschuh R A, Chefd'hotel C, Ziegler S I, Navab N, Schwaiger M and Nekolla S G 2009 Tissue classification as a potential approach for attenuation correction in whole-body PET/MRI: evaluation with PET/CT data *J. Nucl. Med.* **50** 520–6

Mehranian A, Arabi H and Zaidi H 2016 Vision 20/20: magnetic resonance imaging-guided attenuation correction in PET/MRI: challenges, solutions, and opportunities *Med. Phys.* **43** 1130–55

Mehranian A, Zaidi H and Reader A J 2017 MR-guided joint reconstruction of activity and attenuation in brain PET-Mr *NeuroImage* **162** 276–88

Mostafapour S, Gholamiankhah F, Dadgar H, Arabi H and Zaidi H 2021 Feasibility of deep learning-guided attenuation and scatter correction of whole-body 68Ga-PSMA PET studies in the image domain *Clin. Nucl. Med.* **46** 609–15

Schulz V *et al* 2011 Automatic, three-segment, MR-based attenuation correction for whole-body PET/MR data *Eur. J. Nucl. Med. Mol. Imaging* **38** 138–52

Sekine T, Ter Voert E E, Warnock G, Buck A, Huellner M, Veit-Haibach P and Delso G 2016 Clinical evaluation of zero-echo-time attenuation correction for brain 18F-FDG PET/MRI: comparison with atlas attenuation correction *J. Nucl. Med.* **57** 1927–32

Smith L N 2018 A disciplined approach to neural network hyper-parameters: I. Learning rate, batch size, momentum, and weight decayarXiv:1803.09820

Surti S 2015 Update on time-of-flight PET imaging *J. Nucl. Med.* **56** 98–105

Teuho J, Torrado-Carvajal A, Herzog H, Anazodo U, Klén R, Iida H and Teräs M 2020 Magnetic resonance-based attenuation correction and scatter correction in neurological positron emission tomography/magnetic resonance imaging—current status with emerging applications *Front. Phys.* **7** 243

van Sluis J, Boellaard R, Somasundaram A, van Snick P H, Borra R J H, Dierckx R, Stormezand G N, Glaudemans A and Noordzij W 2020 Image quality and semiquantitative measurements on the biograph vision PET/CT system: initial experiences and comparison with the biograph mCT *J. Nucl. Med.* **61** 129–35

Wang T, Lei Y, Fu Y, Curran W J, Liu T, Nye J A and Yang X 2020 Machine learning in quantitative PET: a review of attenuation correction and low-count image reconstruction methods *Phys. Med.* **76** 294–306

Watson C C 2007 Extension of single scatter simulation to scatter correction of time-of-flight PET *IEEE Trans. Nucl. Sci.* **54** 1679–86

Wollenweber S, Ambwani S, Delso G, Lonn A, Mullick R, Wiesinger F, Piti Z, Tari A, Novak G and Fidrich M 2013 Evaluation of an atlas-based PET head attenuation correction using PET/CT & MR patient data *IEEE Trans. Nucl. Sci.* **60** 3383–90

Yang J, Park D, Gullberg G T and Seo Y 2019 Joint correction of attenuation and scatter in image space using deep convolutional neural networks for dedicated brain (18)F-FDG PET *Phys. Med. Biol.* **64** 075019

Zaidi H and El Naqa I 2021 Quantitative molecular positron emission tomography imaging using advanced deep learning techniques *Annu. Rev. Biomed. Eng.* **23** 249–76

Zaidi H, Montandon M-L and Meikle S 2007 Strategies for attenuation compensation in neurological PET studies *Neuroimage* **34** 518–41

Zaidi H, Ojha N, Morich M, Griesmer J, Hu Z, Maniawski P, Ratib O, Izquierdo-Garcia D, Fayad Z A and Shao L 2011 Design and performance evaluation of a whole-body Ingenuity TF PET-MRI system *Phys. Med. Biol.* **56** 3091–106